



Investigation of dual-functional carbon cathode catalysts from agricultural wastes in the heterogeneous electro-Fenton process

Qiang Yang ^{a,b}, Longgang Chu ^{a,b}, Tongliang Wu ^a, Yiyi Zhou ^c, Cun Liu ^a, Long Cang ^a, Guodong Fang ^{a,*}, Peixin Cui ^{a,*}, Yujun Wang ^a

^a Key Laboratory of Soil Environment and Pollution Remediation, Institute of Soil Science, Chinese Academy of Sciences, 210008 Nanjing, PR China

^b University of Chinese Academy of Science, 100049 Beijing, PR China

^c Beijing Construction Engineering Group Environmental Remediation Co. Ltd., 100015 Beijing, PR China

ARTICLE INFO

Keywords:

Biochar
Heterogeneous electro-Fenton
MnO nanoclusters
Dual-functional electro-catalysts
operando XAFS

ABSTRACT

In heterogeneous electro-Fenton process, the design of electrocatalysts for *in-situ* generation of H₂O₂ and efficient conversion to •OH remains a challenge. Herein, a simple one-step pyrolysis strategy has been developed to synthesize green and stable dual-functional electro-catalysts from agricultural wastes. The biochar of soybean roots (RSBC) with ample -COOH and C-O-C functional groups exhibited considerable capacity for H₂O₂ production (21.6 mM at -0.4 V vs RHE), and the dual-functional electron-catalyst exhibits an excellent catalytic reaction for antibiotics removal (100 % cloroquine phosphate with $k_{obs}=0.035\text{ min}^{-1}$). The ultra-small MnO nanoclusters (<2 nm) in the biochar of *Phytolacca americana* leaves (LPBC) were the active center via the transfer of electrons between adsorbed H₂O₂ and Mn atoms to produce reactive •OH, as identified by *operando* X-ray absorption fine structure (XAFS) spectroscopy and density functional theory calculations. This work provides a new direction in the design of dual-functional carbon cathode catalysts for environmental remediation.

1. Introduction

Large-scale use of antibiotic medicines can aggravate aquatic pollution and may pose potential threats to ecosystem stability and ultimately, human health [1,2]. Cloroquine phosphate (CQP) is gaining popularity as a potential treatment for coronavirus disease 2019 (COVID-19). The persistent and bio-accumulative CQP, as antiviral and antibacterial pharmaceutical, might exert potential threat to living organisms and environment due to its high toxicity [3,4]. The ongoing development of efficient and eco-friendly technologies to remove such organic pollutants from the environment is essential. Hydrogen peroxide (H₂O₂) is an environmentally friendly oxidant that can be used in traditional advanced oxidation processes (AOPs) for remediation [5,6]. However, one of the challenges with such AOPs is the sustainable *operando* production of H₂O₂, which is desirable to reduce costs due to storage and transport [7].

Electro-catalytic H₂O₂ synthesis via the two-electron oxygen reduction reaction (2e ORR) pathway has progressed in recent years and appears to be an attractive and feasible method for industrial production of H₂O₂ [8–10]. For the 2e ORR route, electro-catalysts with selective and

active sites are a prerequisite. Carbonaceous materials, including carbon black (CB) [11], carbon nanotubes (CNTs) [6], graphene oxide (GO) [12], and N/S-doped carbon [13–15] have been widely studied as good 2e ORR catalysts for H₂O₂ synthesis, due to the following attributes; (i) the existence of both C-O and C=O functional groups on their surfaces and edges, (ii) hierarchically porous structures with abundant micro-, meso-, or even macro-pores for oxygen transmission, and (iii) good structural stability and electrical conductivity.

Due to the low solubility in H₂O, utilization of O₂ has become a bottleneck in the reaction [16]. Gas diffusion electrode (GDE) use is a promising strategy to improve the mass transfer and utilization efficiency of O₂ since the electrode's hydrophobic surface could provide stable three-phase interfaces on the cathode for ORR [17,18]. Many researchers have successfully fabricated various GDEs using carbonaceous materials as the catalytic layer, to synthesize H₂O₂. With this approach the concentration of H₂O₂ can reach between 10 and 300 mM [19–21]. Based on our previous studies [22,23], biochar products from soybean root wastes (RSBC) are a promising strategy in this field. Unfortunately, investigations into the electro-catalytic H₂O₂ synthesis by biochar products still appears under researched, and thus, the

* Corresponding authors.

E-mail addresses: gdfang@issas.ac.cn (G. Fang), pxcui@issas.ac.cn (P. Cui).



application of such material in the production of H_2O_2 needs further exploration.

In terms of efficient *in-situ* generation of H_2O_2 in the electro-Fenton (EF) process, heterogeneous EF (HEF) has emerged as the state-of-art strategy to convert H_2O_2 into $\bullet\text{OH}$ for refractory organic compound removal [24,25]. The metal atoms on carbon-based materials were considered as the active sites in HEF process, and to increase the utilization of metal atoms in these materials, the size of the metal catalyst could be reduced to below 2 nm due to the quantum size effect on the electronic properties [26,27]. Hyperaccumulators could be used as a class of alternative precursor materials to synthesize carbon-based catalysts since they provide two critical properties: i) endogenous transition metals in the biomass; ii) ample heteroatoms, such as N, O, S, and P, which are able to stabilize metal atoms against aggregation [28].

Phytolacca americana is the first known herbaceous Mn hyperaccumulator globally [29]. It can accumulate up to 14,477 mg kg^{-1} Mn in its leaf when growing naturally [30]. Using X-ray absorption spectroscopy, it was shown that 90 % of the Mn in the leaf was present in the form of Mn(II), with strong evidence of the role of carboxylic acids, such as malate or citrate, as complexing ligands [31,32]. The utilization for hyperaccumulator biomass is required to reduce the potential risk of secondary contamination and the synthesis of biochar by pyrolysis or hydrothermal carbonization is the most common method [33]. Benefiting by the porous microstructure and high concentration and dispersion of metal ions, biochar derived from hyperaccumulator biomass has been used to capture carbon dioxide [34], immobilize heavy metals [35,36] and degradation organic pollutants [28]. Therefore, *P. americana* could be a natural precursor for the development of a carbon-based Mn catalyst, and thus has great potential in reducing the cost of relevant and environmentally friendly pollution remediation.

In this work, biochar from soybean root wastes was prepared and used as GDE for electro-catalytic H_2O_2 synthesis and ultra-small Mn nanoclusters with high catalytic activity were introduced into the GDE via pyrolysis of the Mn hyperaccumulator *P. americana* (LPBC) leaf, which is a beneficial attempt on the utilization of agricultural wastes. Cloroquine phosphate (CQP) was selected as a model pollutant to evaluate the performance of the mixture biochar GDE in the HEF system and the particular contributions of RSBC and LPBC were evaluated. Furthermore, the molecular mechanisms of outstanding HEF activities of ultra-small MnO nanocluster sites were investigated via high-angle annular dark field scanning transmission electron microscopy (HAADF-STEM), as well as *ex-situ* and *operando* X-ray absorption fine structure (XAFS) spectroscopy and density functional theory (DFT) calculations.

2. Materials and methods

2.1. Materials

Phytolacca americana was grown in a greenhouse with irrigation of 100 mL water containing 10 mM MnCl_2 once every two days to have a high concentration of Mn without damage of the plant. The leaf of *P. americana* was washed, divided into small pieces, dried and smashed with a crusher after harvest. For comparison, the counterparts of Mn-free *P. americana* were also obtained in the absence of irrigation Mn. The soybean root was obtained from Nanjing, Jiangsu Province, China. Cloroquine phosphate (CQP), and Rhodamine B (RhB) were purchased from Aladdin (Shanghai). The 5,5-Dimethyl-1-pyrroline-N-oxide (DMPO), 2,2,6,6-Tetramethyl-4-piperidone hydrochloride (TEMP) were purchased from Dojindo Laboratories, Kumamoto (Japan). Carbon felt (Beijing, Jinglong), PTFE, and carbon black (CB) (Shanghai, Hesen) were used for GDE preparation. Milli-Q ultra-pure water (Millipore, USA) was used in the preparation of all reaction solutions. All chemicals used in this study were analytical grade.

2.2. Synthesis of biochar

The prepared leaves of *P. americana* containing Mn were pyrolyzed at 300 °C for 1 h at a heating rate 1 °C min^{-1} , then increased to 500 °C for 4 h at the same heating rate in a tube furnace with a high-purity N_2 atmosphere and a flow rate of 30 mL min^{-1} . The resulting black powder was named LPBC. The Mn-free dried and ground leaf of *P. americana* had exogenous $\text{MnCl}_2 \cdot 4 \text{ H}_2\text{O}$ (with the addition mass determined by the content of endogenous Mn in the biomass) was also pyrolyzed at 500 °C under the same conditions, with the final product named as LPBC-exo.

The dried and smashed root of soybean was pyrolyzed at 300 °C for 1 h at a heating rate of 1 °C min^{-1} , which was then increased to 700 °C for 4 h at the same heating rate in a tube furnace with a high-purity N_2 atmosphere and a flow rate of 30 mL min^{-1} . The final solid product was named RSBC.

2.3. Fabrication of GDE

After ultrasonic cleaning in ethanol for 15 min, the CF (2.5 or 10 mm thick) was soaked in PTFE suspension (5 %) for a further 30 min with ultrasonic treatment, dried, and then calcined at 360 °C for 30 min at an increasing rate of 5 °C min^{-1} in a high-purity N_2 atmosphere and a flow rate of 30 mL min^{-1} . Following this, 40 mg RSBC, 10 mg CB, 5 mL absolute ethyl alcohol, and 50 μL PTFE suspension were mixed with ultrasonic treatment for 15 min and then uniformly coated on the surface of CF as the catalyst layer. Finally, the electrodes loaded with the catalytic layer were calcined at 360 °C for 30 min at 5 °C min^{-1} in a high-purity N_2 atmosphere and a flow rate of 30 mL min^{-1} [11].

2.4. Fabrication of dual-functional electro-Fenton catalyst

The mixture of 15 mg LPBC, 25 mg RSBC, 10 mg CB, 5 mL absolute ethyl alcohol, and 50 μL PTFE suspension were uniformly coated on the surface of CF as the catalyst layer. The electrodes loaded with the catalytic layer were calcined at 360 °C for 30 min at 5 °C min^{-1} in a high-purity N_2 atmosphere and a flow rate of 30 mL min^{-1} .

2.5. Characterization

The samples were characterized by scanning electron microscopy (SEM, Genimi500, USA), high-resolution transmission electron microscopy (HR-TEM, JEOL JEM-2100 F, Japan), aberration-corrected HAADF-STEM (JEOL JEM-ARM2000CF, Japan), Brunauer-Emmett-Teller, (BET, Micromeritics Instrument Corporation, Norcross, GA, USA), X-ray diffraction (XRD, Rigaku Ultima), and X-ray photoelectron spectroscopy (XPS, Thermo VG ESCALAB 251XI). The metal content was determined by inductively coupled plasma optical emission spectrometry (ICP-OES). Electron paramagnetic resonance (EPR) analysis of free radicals trapped by DMPO and TEMP were conducted using a Bruker E580 spectrometer (Germany).

The XAFS spectra at the Mn K-edge of LPBC and references were collected at beamlines BL14W1 and BL11B in Shanghai Synchrotron Radiation Facility (SSRF) and Beijing SCISTAR Co. Ltd. (experimental details in Text S1). Density functional theory calculations are listed in Text S2.

2.6. Electrochemical performance

Electro-catalytic H_2O_2 production was performed on a CHI 660 A electrochemical station (Chenhua Instrument Co. Ltd., China) in a 100 mL single-compartment reactor, using GDE (1 cm \times 1.5 cm) as the cathode and DSA (2 cm \times 4 cm; IrO_2 coating) as the anode, $\text{Hg}/\text{Hg}_2\text{SO}_4$ or Ag/AgCl as the reference electrode, and with the applied potential normalized to the reversible hydrogen electrode (RHE). Na_2SO_4 (0.05 M) was used as the supporting electrolyte. The pH of the electrolyte was adjusted with H_2SO_4 (0.1 M) and NaOH (0.1 M). The potentials

measured in this work were calibrated to the RHE via the equations:

$$E_{RHE} = E_{Ag/AgCl} + 0.0591 \text{ pH} + 0.197 \text{ V}$$

$$E_{RHE} = E_{Hg/Hg_2SO_4} + 0.0591 \text{ pH} + 0.656 \text{ V}$$

The reactor and electrodes used in the degradation experiments were the same as those used in the above experiments. The HEF experiments were carried out for degrading CQP and RhB at a concentration of 20 mg L⁻¹. More details are provided in Text S3.

The concentration of CQP was analyzed by UV-vis spectrophotometer (UV-2700, Shimazu Co. Ltd, Japan) at a wavelength of 343 nm. The concentration of RhB was determined using UV-vis spectrometer at a wavelength of 554 nm. Electron paramagnetic resonance (EPR, Bruker E500-9.5/12, Germany) spectrometry was conducted to identify the free radicals in the experiments. Total organic carbon (TOC) was measured with a Vario Select TOC (Elementar, Germany). The degradation products of CQP were analyzed by liquid chromatography-time-of-flight-mass spectrometry (AB XR500, LC-QTOF) equipped with a UV-Vis detector and Eclipse Plus C18 column. The mobile phases were acetonitrile and 0.1 % formic acid (10/90, v%/v%) with a flow rate of 0.8 mL min⁻¹ and a column temperature of 30 °C [37]. The injection volume was 10 µL.

3. Results and discussion

3.1. Characterization of carbonaceous materials

The elemental content of RSBC and LPBC are listed in Table S1. The amount of Mn loaded in LPBC was 36.5 mg g⁻¹ according to the ICP-OES results. As shown in Fig. 1a, the XRD spectrum of RSBC presented two broad peaks at the 2θ ranges of 20–30° and 40–45°, which are the characteristic peaks of the (002) and (001) planes of graphitic carbon, respectively. The characteristic peaks of SiO₂ and KCl could be detected but no obvious peaks associated with Mn-based metallic or metal oxides were detected in the XRD spectra of LPBC since Si, K, and Cl are both essential elements for plant growth [38]. The surface area analysis (BET) for the two prepared samples are displayed in Fig. 1b, c and Table S2. The BET surface areas of RSBC and LPBC were 391.1 and 470.2 m² g⁻¹, respectively. In addition, micro-pore area was dominant on the BET surface, demonstrating that the as-prepared biochar products possessed desirable specific surface area and porosity [39,40].

The morphologies of RSBC and LPBC were observed by SEM and HR-TEM. Scanning electron microscopy images showed typically rough and porous surface texture, with micro-pores diameter of around 10 µm evenly distributed on the surface of both RSBC and LPBC (Fig. 1d and f). This implies high potential for promoting mass transfer efficiency during 2e ORR [20]. In the HR-TEM images, an ordered graphitic structure was observed on the edge of RSBC-700 (Fig. 1e), suggesting that defects (attributed to carbon atoms no longer in the regular tubular structure) may exist in the carbon materials [41]. Two characteristic peaks located at 1350 (D band) and 1580 (G band) cm⁻¹ were related to the defective or disordered graphitic structures (Fig. S1). RSBC obtained by higher temperature pyrolysis has a higher degree of graphitization (lower I_D/I_G) than LPBC. Highly graphitic carbon will facilitate the electron conductance and enhance the anti-corrosion capability of the carbon matrix, thereby enhancing the long-term operation stability. It has been reported that such defects in the carbon matrix may act as reactive sites for oxygen adsorption or reduction during the 2e ORR process [42,43]. In the HR-TEM images of LPBC in Figs. 1g and S2, no metallic nanoparticles (NPs) were observed, and elemental mapping revealed a uniform distribution of C, N, and Mn species across the biochar. The atomic dispersion of Mn was further indicated by HAADF-STEM (Figs. 1i and S3), where the bright spots correspond to Mn atoms homogeneously dispersed throughout the biochar. No obvious aggregates were observed, suggesting that Mn atoms predominantly existed in forms of either single atoms or ultra-small nanoclusters. In comparison, LPBC

with exogenous MnCl₂·4 H₂O (LPBC-exo) showed an obvious aggregation of Mn nanoparticles in the target size range of 10–100 nm (Figs. S4 and S5). These differences imply that hyperaccumulators may be able to be exploited as a class of alternative raw materials to synthesize carbon-based catalysts (Fig. 2a).

Surface sensitive XPS was conducted to better understand the surface chemical environment of RSBC and LPBC (Fig. S6). The high-resolution C 1 s spectrum could be deconvoluted into the following bands: C-C in the carbon matrix at 284.5 eV, defects eV (C atoms exist in incomplete tubular structure) [41], C-O at 286.2 eV, -COOH at 288.5 eV, and the characteristic shakeup line of carbon in aromatic compounds at 290.3 eV ($\pi-\pi^*$ transition) (Figs. 2b, and S7a). The O 1 s spectrum consisted of four peaks with binding energies at 530.8, 531.6, 532.5, and 533.7 eV, which can be assigned to C=O, C-OH, C-O-C, and -COOH (Fig. S7b) [43]. These results indicate that the suitable pyrolysis producers based on our previous studies [28] induced more oxygen-containing functional groups. In general, adsorbed O₂ acts as a scavenger for excess electrons originating from donor-specific sites, such as oxygen vacancies (OVs), nitrogen vacancies (NVs), and hydroxyl groups (-OH) [44]. To further understand the vacancies in RSBC, EPR was employed. As shown in Fig. S8, an obvious EPR signal was observed at g = 2.003, which was ascribed to the electrons trapped in the OVs on the graphite-like architecture. This demonstrates that oxygen (O₂) may be easily trapped in the OVs for further reduction. The high-resolution N 1 s XPS of LPBC could be deconvoluted into three characteristic peaks (Fig. 2c); pyridinic N at 398.4 eV, Mn-N at 399.1 eV, and pyrrolic N at 400.8 eV, in which the Mn-N peak suggested a strong interaction between Mn and N atoms against aggregation [45,46]. Two fitting peaks of Mn 2p_{3/2} located at 641.2 eV and 642.8 eV were attributed to Mn(II) and Mn(IV) (Fig. 2d), respectively.

To further verify the local electrochemical and atomic structures of Mn sites in LPBC, *ex-situ* XAFS spectra were collected. In the leave of *Phytolacca americana*, Mn atoms are chelated with carboxyl groups of acetic acid to form Mn oxalate (Fig. S9). The Mn oxalate disperses in the vacuole and cytoplasm, avoiding the aggregation of Mn atoms. The normalized Mn K-edge X-ray adsorption near edge structure (XANES) spectrum of LPBC and references are shown in Fig. 2e. The absorption edge of LPBC was located between that of MnO and Mn₂O₃, suggesting that Mn in LPBC was a mixture of Mn(II) and Mn(III). The valence of Mn in LPBC was determined as + 2.24, since there is a linear relationship between the position of the absorption edge and Mn valences (Fig. S10). This suggested Mn(II) was the main form of Mn in LPBC. The extended X-ray absorption fine structure (EXAFS) spectra were further analyzed to examine the atomic structure around Mn. In the Fourier transformed R space (Fig. 2f), there were three main peaks attributed to the Mn-O/N, Mn-O/N and Mn-Mn coordination, respectively. The two Mn-O/N shells with different bond lengths come from different coordination structure, demonstrating Mn atoms existed as a mixture of Mn single-atoms and ultra-small MnO clusters. The total coordination number of two Mn-O/N shell was 4.8 (1.6 + 3.2) as shown in Table S3. Considering the common coordination numbers are 4 and 6 in Mn single-atoms and MnO, respectively, and the weighted average coordination numbers in the mixture, about 40 % of Mn atoms aggregated to MnO clusters while the rest was in single atom form. The detailed EXAFS fitting results of LPBC and references are listed in Table S3. In the wavelet transformed pattern of LPBC and the reference materials shown in Figs. 2g and S11, two main intensity maximum areas are well-resolved at 4.5 and 7.0 Å⁻¹, attributed to the Mn-O/N and Mn-Mn coordination, respectively. The intensity of the Mn-Mn peak in LPBC was quite weak compared with MnO, which further indicates that there is only minor aggregation of Mn atoms as MnO.

3.2. The productivity of H₂O₂

Oxygen-containing functional groups, graphitization degree and porosity of biochar have been proved to be the key factors for efficient 2e

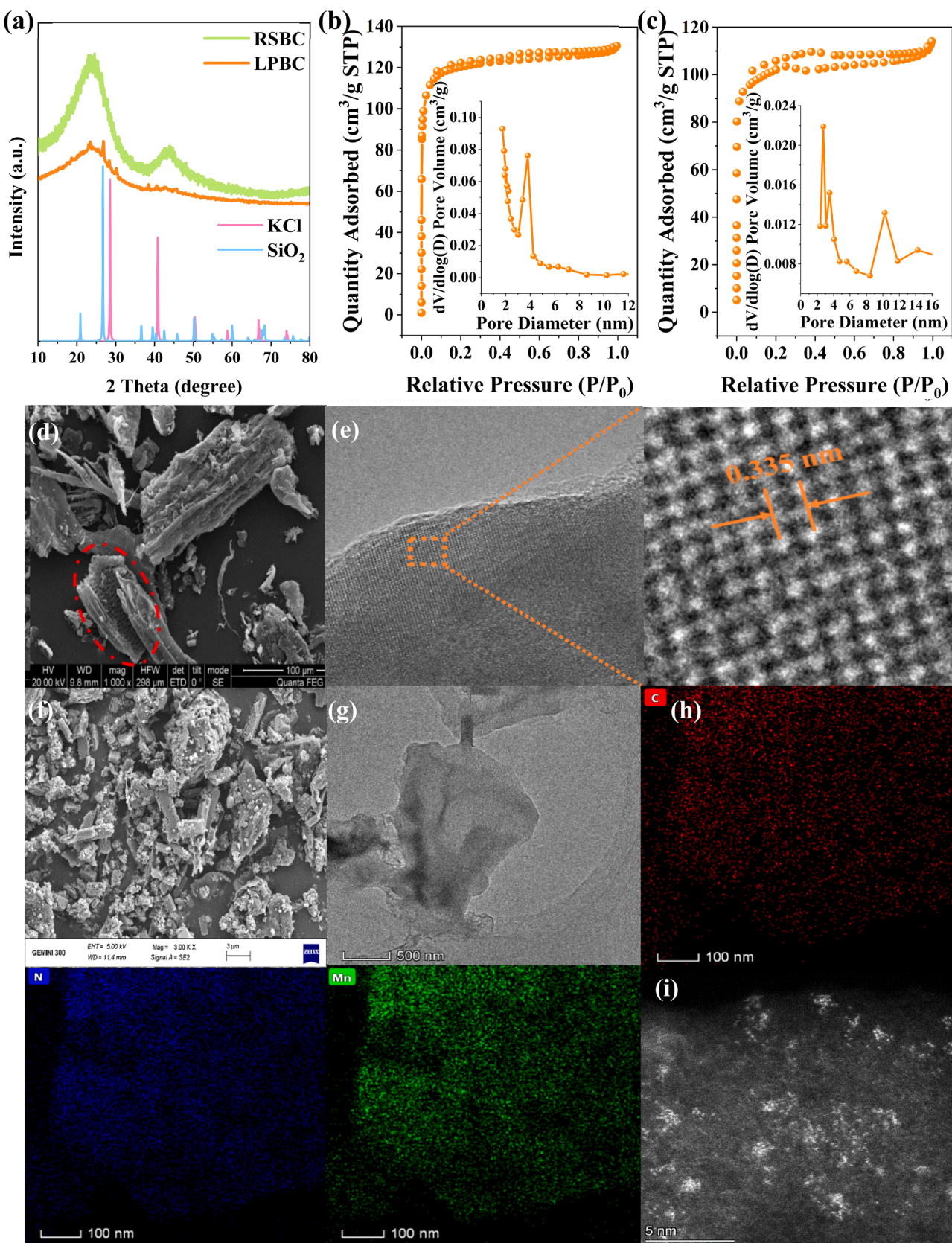


Fig. 1. (a) XRD pattern, (b,c) nitrogen adsorption-desorption isotherm and pore size distribution of RSBC and LPBC (d) SEM, and (e) HR-TEM images of RSBC, (f) SEM, (g) HR-TEM, (h) elemental mapping, and (i) HAADF-STEM images of LPBC.

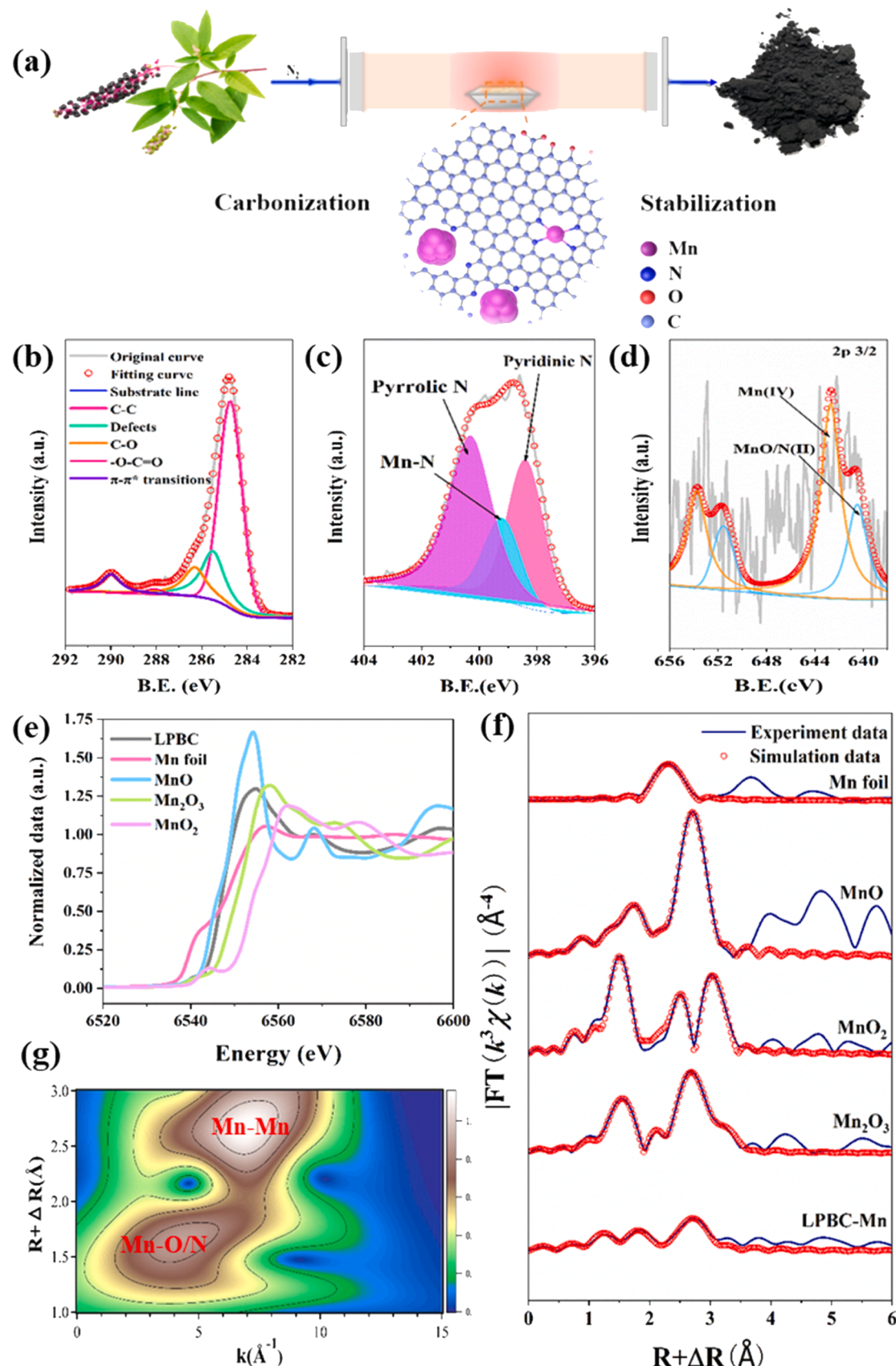


Fig. 2. (a) Schematic of LPBC preparation via pyrolysis, (b, c, d) high-resolution XPS spectra of C 1 s, N 1 s, and Mn 2p in LPBC, (e) Mn K-edge XANES of LPBC and references, (f) NEXAFS spectra of Mn and references, (g) the corresponding WT-EXAFS plot of Mn in LPBC.

ORR [47]. According to BET, SEM and HR-TEM results provided in the previous section, RSBC has significant potential as the catalytic layer in GDE for hydrogen peroxide (H_2O_2) synthesis. As displayed in Figs. 3a and S12, the cumulative concentrations of H_2O_2 were 12.1 mM, 19.9 mM, and 24.2 mM at the potential range of 0 V to -0.6 V vs. RHE when using RSBC as a catalyst for GDE, respectively, noticeably outperforming that of a pure CF system. The high catalyst activity for H_2O_2 synthesis can be attributed to the C-O-C and -COOH functional groups at the edge of the graphene [6], in accordance with the XPS results.

The current efficiency (CE) was used to evaluate the 2e ORR efficiency in the reaction (Fig. 3b). The CE reached over 80 % in the first 30 min and then gradually decreased to 43% with working hours because of the penetration of the catalytic layer by electrolyte. The high H_2O_2 production yield and current efficiency suggested that RSBC was an outstanding catalytic layer in GDE for H_2O_2 synthesis.

The performance of RSBC for H_2O_2 synthesis was further investigated under different conditions. The performance of RSBC with different pH conditions was also examined. As displayed in Fig. S13, even in extreme alkaline conditions, the catalyst still exhibited a modest reactivity for 2e ORR, which indicates the potential for the removal of organic pollutants across a wide range of pH during the HEF process.

Furthermore, the working stability of the GDE was also evaluated up to 24 h. The concentration of H_2O_2 was maintained at around 30 mM after 120 min reaction (Fig. 3c), which demonstrated that as-prepared GDE could be applied for practical HEF processes. To evaluate the ORR activity of the catalytic layer, the linear sweep voltammetry (LSV) plots of GDE loaded with different catalytic layers were examined (Fig. S14). With the cathode potential shifting negatively, the current response gradually increased. Compared with the original CF, the RSBC exhibited the highest current response (Fig. S15). As discussed before, 2e ORR is more advantageous on carbon substrates with a higher level of graphitization. RSBC obtained by higher temperature pyrolysis has a higher degree of graphitization (lower I_D/I_G), which is able to facilitate the electron conductance and enhance the anti-corrosion capability of the carbon matrix. However, the concentration of H_2O_2 decreased from 23.9 mM to 2.53 mM when the cathode included a coated layer of LPBC as catalyst, suggesting a different behavior of LPBC in H_2O_2 production.

The ORR performance was evaluated on a rotating ring-disk electrode (RRDE) at 1600 rpm in an O_2 -saturated 0.1 M Na_2SO_4 electrolyte [48]. Fig. 3d shows the polarization curves for RSBC, and RSBC+LPBC, with the oxygen reduction current recorded on the disk electrode and the H_2O_2 oxidation current on the Pt ring electrode. LSV curves indicate

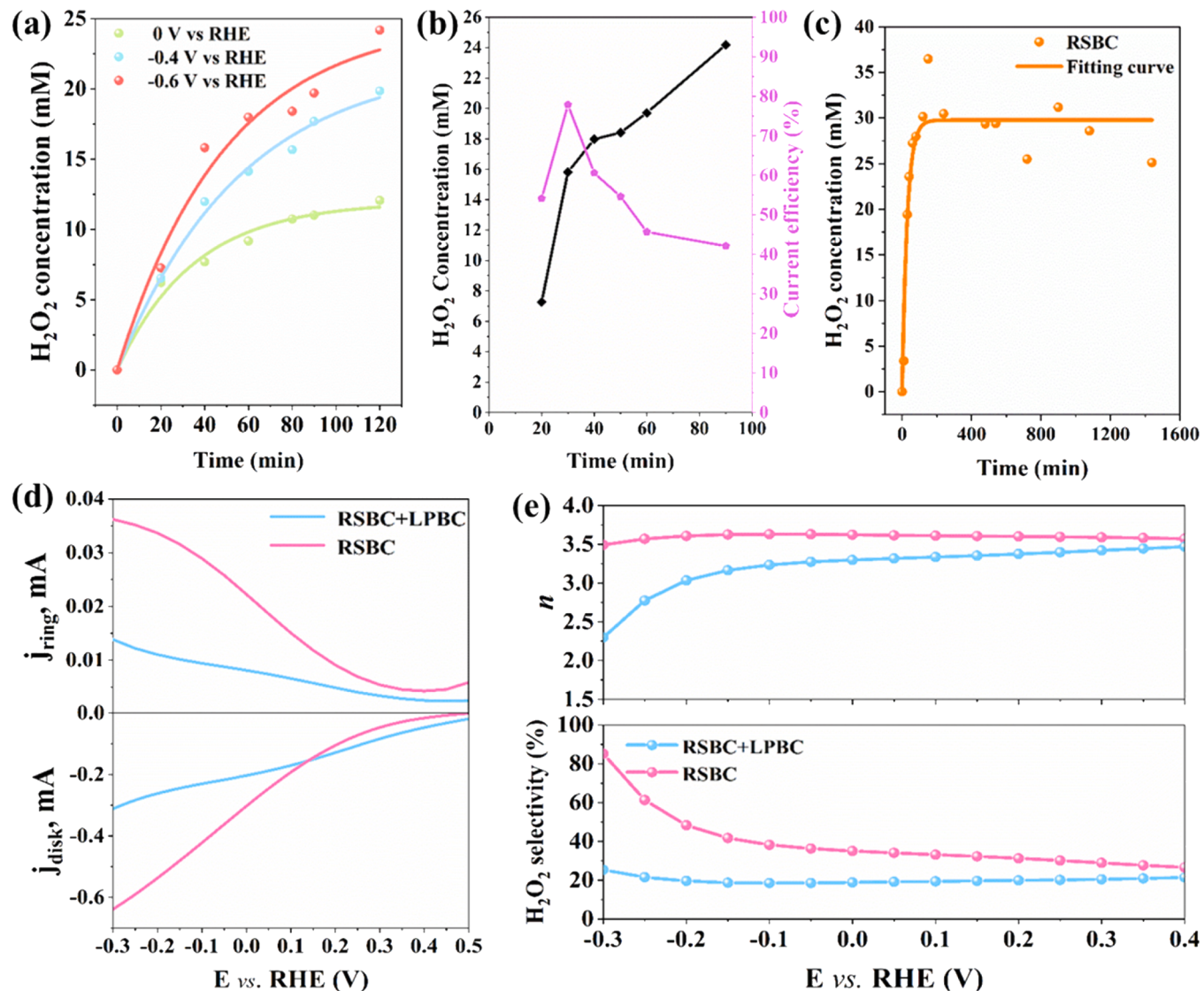


Fig. 3. (a) The concentrations of H_2O_2 at different applied potentials, (b) current efficiency at -0.4 V vs RHE, (c) H_2O_2 concentration in DC power mode for the long-term stability test with $E = 2.8$ V, $A = 120$ mA, $\text{pH} = 3$, $[\text{Na}_2\text{SO}_4] = 0.05$ M, (d) LSV curves of RSBC and RSBC+LPBC on RRDE collected at a rotation speed of 1600 rpm and a scan rate of 5 mV s^{-1} in 0.1 M Na_2SO_4 , (e) H_2O_2 selectivity and electron transfer number calculated from the LSV curves.

a ring current (j_{ring}) of 0.0138 mA and disk current (j_{disk}) of -0.3118 mA for RSBC+LPBC at -0.3 V vs. RHE, which was much lower than that of RSBC (0.0362 mA and -0.6384 mA). Compared with the presence of RSBC+LPBC, RSBC displayed the highest oxygen reduction current and modest positive onset potential (0.509 V vs. RHE) at the disk electrode, indicating excellent ORR activity. The H_2O_2 selectivity (%) and average number of electrons transfer (n) were calculated from the disk and ring currents of RRDE. As shown in Fig. 3e, the RSBC delivers an excellent H_2O_2 selectivity (%) of over 85 % and an electron transfer number (n) of 2.2 with the applied potential at 0.4 V vs. RHE. Contrasting with this, the H_2O_2 selectivity (%) of RSBC+LPBC was less than 25.4 % at the same applied potential with n larger than 3.5, respectively. The results of these ORR tests indicate that carbon-based materials originating from the chosen biomass can also be utilized as promising catalysts for electro-catalytic H_2O_2 synthesis via the 2e ORR pathway. Moreover, the Mn sites in LPBC were able to change the apparent ORR process from the 2e to the 3 or 4e pathway.

3.3. CQP degradation by the HEF process

The CQP degradation was conducted in a single-cell reactor, using RSBC as catalyst loading on the cathode for H_2O_2 production. Only 54.6 % CQP was degraded in 100 min (Fig. 4a), suggesting that a high concentration H_2O_2 synthesized by the 2e ORR could not effectively degrade CQP without activation. The observed degradation may be attributed to the existence of OVs in RSBC since O_2 is thermodynamically able to capture electrons from OVs to form reactive oxygen species

(ROSS) [49]. In contrast, the final removal rate of CQP was 100 % in the presence of LPBC as the electro-catalyst. As reported before [50], the heterogeneous catalyst plays a vital role in converting H_2O_2 into ROSS in the HEF process, which explains the further influence of LPBC on CQP removal that was detected. To verify the role of Mn single-atoms and ultra-small MnO nanoclusters in the HEF process, KSCN was applied as a poisoned reagent to shield the Mn sites because SCN^- can form a stable chelate complex with metal-unsaturated sites, thus curing the catalysis [51,52]. With addition of KSCN, the CQP degradation curve was almost the same as that of the control treatment, suggesting that the Mn sites played a critical role in the improved HEF process. The corresponding apparent kinetic constants are displayed in Fig. 4b.

The control experiments of pristine GDE (pure CF) and addition of Mn^{2+} were also conducted to exclude the effects of anode oxidation and aqueous Mn^{2+} on CQP removal. As shown in Fig. 4a, c, the final removal rates of CQP under these conditions were 14.1 % and 15.6 %, respectively. We evaluated the catalytic performance under different interfering factors, such as, adding methanol and inorganic ions in natural water (Table S4). The CQP degradation efficiencies still reached 85.3 % and 80.3 % while maintaining excellent kinetic performance (Fig. 4c, d). As shown in Fig. S16, kinetic performance of LPBC was 3.5 times higher than that of the LPBC-exo HEF system, further indicating the excellent catalytic activity of ultra-small MnO nanoclusters.

The influence of the applied potentials and the initial electrolyte pH value on CQP removal were investigated. As displayed in Fig. S17, the removal rate of CQP within 100 min was 91.6 %, 98.6 % and 100 % when the applied potential was set at 0 V, -0.4 V and -0.6 V vs RHE,

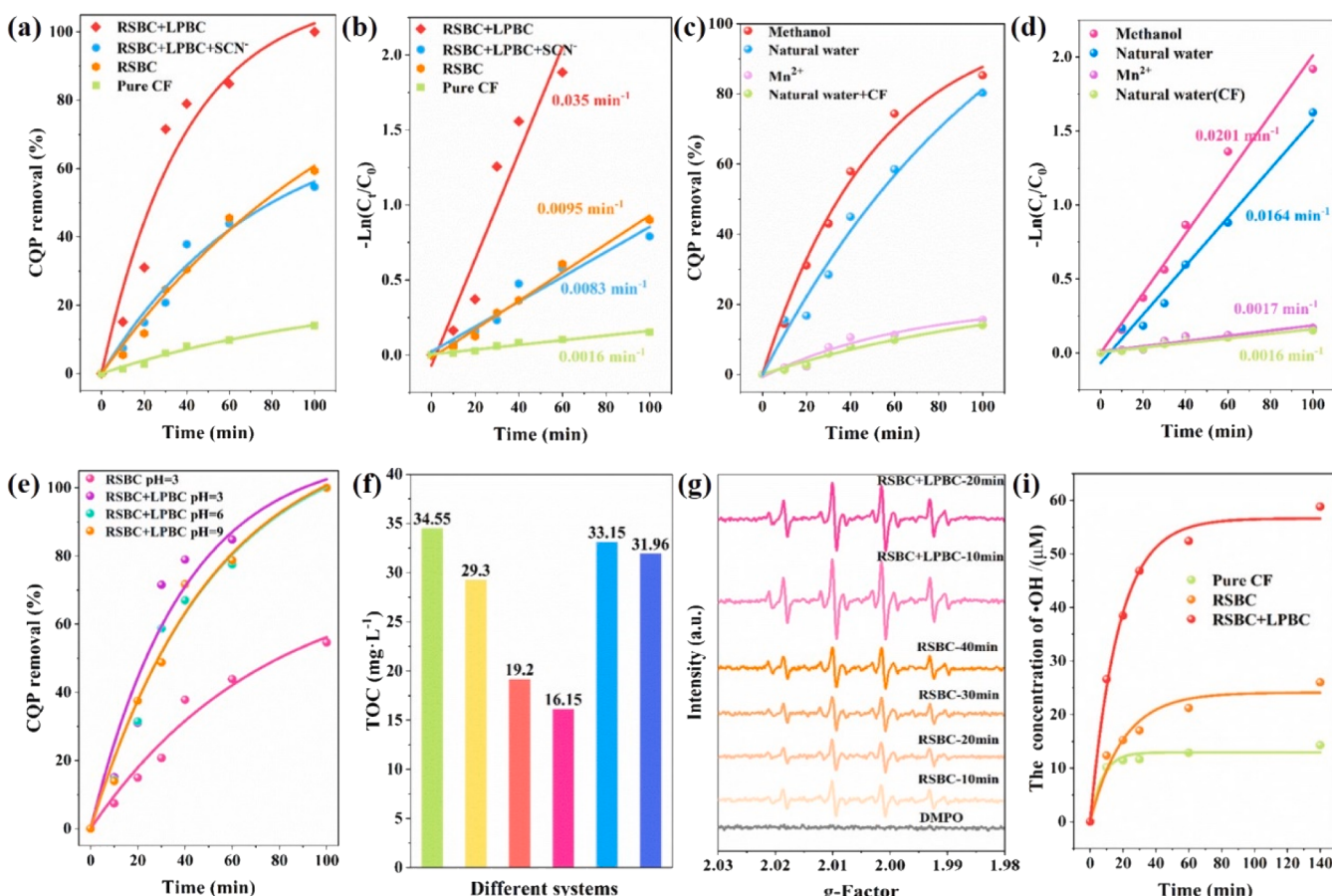


Fig. 4. (a, c) CQP removal rates (b, d) corresponding kinetic constants in the HEF process, (e) effect of different pH conditions on CQP degradation, (f) TOC values in different systems, pure CF (green), RSBC (yellow), RSBC+LPBC (pH=3) (orange), RSBC+LPBC (pH=6) (pink), RSBC+Mn²⁺ (light blue), RSBC+LPBC+SCN⁻ (dark blue) in natural water, (g) EPR signals of time-varying DMPO-OH in RSBC and RSBC+LPBC systems, (h) the concentrations of •OH in pure CF, RSBC, and RSBC+LPBC system; -0.4 V vs RHE, 0.05 M Na_2SO_4 .

respectively. The initial pH plays an essential role in catalytic performance of the heterogeneous process since wastewaters can vary widely in pH. As shown in Fig. 4e, regardless of pH variation, 100 % of CQP removal could be achieved in the RSBC+LPBC HEF system, which can be attributed to the synergistic effect of the maximized utilization of Mn atoms and the neighboring active sites of -COOH or C-O-C functional groups on the graphitic structure. The contents of Mn in LPBC after acid treatment (1 M H₂SO₄ for 4 h) are displayed in Table S5. When the Mn content in LPBC is lower by half following acid washing, the degradation efficiency ($k_{obs}=0.018 \text{ min}^{-1}$) is also reduced by half (Fig. S18). According to the EXAFS fitting results in Table S3, there are almost one half MnO cluster and one half Mn single-atoms in LPBC, suggesting that the MnO nanoclusters and Mn single-atoms have a nearly catalytic activity.

The detectable leaching of Mn ions was only 0.38 mg·L⁻¹ at pH= 3 during the whole reaction process, and this decreased to less than 0.07 mg·L⁻¹ in neutral and alkaline conditions, demonstrating the stability of LPBC in the whole HEF process of 24 h. Furthermore, as an important indicator to assess the mineralization ability of organic pollutants, the HEF process was used to investigate the TOC values in natural water. As shown in Fig. 4f, the TOC values decreased to 19.2 mg·L⁻¹ and 16.15 mg·L⁻¹ in acid and neutral conditions with considerable mineralization rates of 50 % and 58 %, respectively, when the surface of GDE was coated by a layer of RSBC+LPBC as the catalyst. In contrast, the TOC values were 38.4 mg·L⁻¹ and 29.3 mg·L⁻¹ when using pristine CF and RSBC as catalyst in the cathode, respectively. Consistent with results of CQP degradation efficiency in the presence of Mn²⁺ and SCN⁻, the TOC values reached maximums of 33.15 mg·L⁻¹ and 31.96 mg·L⁻¹ with minimal mineralization rates of 13.6 % and 16.8 %, respectively.

The high TOC removal efficiency in the HEF process suggested that most CQP was oxidized and then transformed into CO₂ or inorganic ions. Additionally, the color of 5–20 mg·L⁻¹ RhB faded rapidly on the surface of GDE within 30 s (Video S1–2), which demonstrated that this HEF system exhibited a very high capacity for dye degradation. Table S6 provides a summary of the recently reported heterogeneous electro-Fenton catalysts for the degradation of pollutants and shows that MnO nanoclusters and Mn single atoms have excellent catalytic activity.

3.4. Catalytic mechanism of the HEF process

The ROSs for CQP removal were measured by EPR spectroscopy with 5,5-dimethyl-1-pyrroline-N-oxide (DMPO) and 2,2,6,6-Tetramethyl-4-piperidone hydrochloride (TEMP) as trapping agents [53]. The time-resolved DMPO-·OH signals (quadrupole peaks with the intensity of 1:2:2:1) in the 2e ORR system quickly became saturated and remained constant from 10 min to 40 min (Figs. 4g and S19), while the intensity of DMPO-·OH signals rapidly increased in the presence of LPBC. However, the time-resolved TEMP-¹O₂ signals (triple peak with the intensity of 1:1:1) were not detected whether LPBC was added into the 2e ORR system or not (Fig. S20). This suggests that ¹O₂ was absent and ·OH was the sole ROS for the removal CQP in the HEF system. Additionally, although methanol can specifically scavenge ·OH ($k_{MeOH \cdot OH} = 9.7 \times 10^8 \text{ M} \cdot \text{s}^{-1}$) [54], the kinetic process of CQP degradation was not strongly influenced by the addition of methanol into the HEF reaction. The reasons why adding methanol cannot effectively inhibit degradation efficiency are as follows: i) methanol is insufficient to quench the hydroxyl radicals that are constantly generated at the cathode, ii) chloroquine molecules (positive charge) may be concentrated on the surface of the cathode rather than in bulk solution, promoting CQP removal efficiency in the HEF system.

To further assess the catalytic performance of LPBC in the HEF system, the concentrations of ·OH in the different treatments were quantitatively detected by using terephthalic acid (TPA) as a chemical molecular probe [55]. As displayed in Fig. 4i, the concentrations of ·OH gradually increased to 12.8 μM and 20.58 μM when using pristine CF and RSBC as the cathode, respectively, while the concentration of ·OH

rapidly accumulated to 58.81 μM during the whole reaction in the RSBC+LPBC system. This was approximately three times higher than in the RSBC treatment. Additionally, the concentration of H₂O₂ decreased from 23.9 mM to 2.53 mM when the cathode included a coated layer of LPBC as catalyst (Fig. S21). The result of the chemical probe experiment further confirmed that LPBC plays a critical role in converting H₂O₂ to ·OH.

To further explore the key role Mn sites played in the HEF process at the atomic level, *operando* XAFS was employed as shown in Figs. 5a and S22. The positions of the absorption edge moved slightly towards higher energy with the increased cathode voltages. It is notable that generally metal is reduced at the cathode and is less positive at high voltage. The increased valence state of Mn in our work may have resulted from Mn not being involved in the 2e ORR process but still able to convert H₂O₂ into ·OH due to the excellent catalytic activity of Mn sites and the wide distribution on carbon matrix. The absorption edge shifted back after the HEF reaction, indicating that the increase of Mn valence comes from the HEF reaction rather than adsorbed hydroxyl groups and the Mn sites has a high stability (Fig. 5b). The EXAFS fitting results revealed that the Mn-O/N coordination numbers of the operando sample in the HEF reaction became higher compared with the pristine sample (Table S3 and Fig. S23), confirming the interaction between Mn atoms and H₂O₂/O₂. Moreover, the coordination structure returned after the HEF reaction, demonstrating again the stability of the Mn sites. The wavelet transformed patterns of all operando samples exhibited two main intensity maximum areas at 4.5 and 7.0 Å⁻¹ (Fig. S24), attributed to structure stability.

Spin-polarized density functional calculations were carried out to elucidate the reaction mechanism of the ultra-small MnO nanoclusters with excellent catalytic activity. According to the best-fitting EXAFS results, N-doped graphene, Mn-N₄ single-atom sites and MnO nanoclusters anchored by an N atom on the plane of graphene were adopted in the calculations (Fig. S25). First, Bader charge analysis was conducted, which represents the charge difference upon the catalysts' surface. In the pristine N-doped graphene, the N atom was negatively charged via withdrawing electrons (+0.694e) from the adjacent C atoms (Fig. S26), thus it may have served as the “adhension strength” sites that anchored metal atoms or nanoclusters during the pyrolysis process [56]. The calculated binding energy between Mn and N in the model 3 was 13.16 eV, demonstrating the strong metal-support interaction (MSI) effect between the MnO nanocluster and the substrate, which is of vital importance in both the catalysis performance and stability for metal-based catalysts.

The adsorption energy of O₂ on different configurations are given in Table S7. In the case of O₂-adsorbed catalyst surfaces, the amount of transferred charge of Mn in model 2 and model 3 is – 1.34 e and – 19.72 e (Figs. S27–S29), respectively. However, Mn becomes more positive by donating electrons to the surface (+0.12 e and +0.71 e respectively for model 2 and 3) when converting H₂O₂ into ·OH. The calculated density of states of N, O p orbitals and Mn d orbitals are plotted in Figs. S30 and S31, which reveals the asymmetric DOS between the spin-up and spin-down channel in the spin-polarized systems (Mn-N SAC, and MnO nanocluster, O^{*} and OH^{*}). There is significant overlapping between Mn DOS and N and O DOSs in the energy range of – 10–0 eV, implying a strong orbital hybridization between Mn d orbitals and N and O p orbitals [57]. These results may indicate that O₂ may have been rapidly converted into ·OH through the reduction and activation process via the synergistic effect of the maximized utilization of Mn atoms and the neighboring active sites of -COOH functional groups on the graphitic structure for O₂ adsorption. Since oxygen electro-reduction to ·OH comprises several elementary reaction steps (Eqs. 1–5) [6,7,58], free energy diagrams of each elementary reaction were analyzed under different active center models and different electrode potentials (Figs. 5c and S2). O₂ is firstly adsorbed on the surface active sites (*) of -COOH or C-O-C [Eq. (1)], then the *O₂ is reduced and protonated to *OOH as the intermediate [Eq. (2)], and *H₂O₂ is subsequently generated [Eq. (3)].

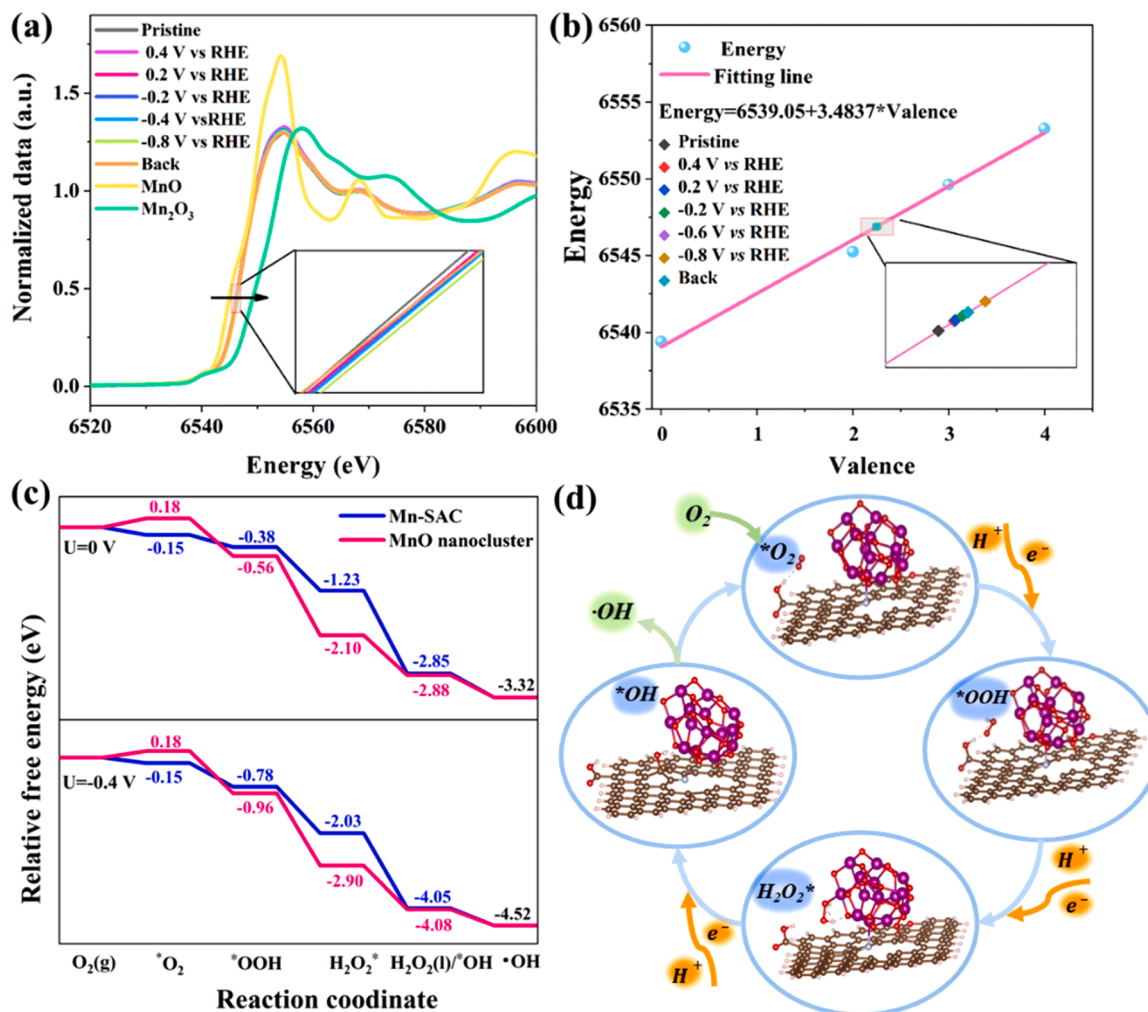


Fig. 5. (a) Operando Mn K-edge XANES, (b) the linear relationship between positions of adsorption edge and Mn valences for LPBC under different applied potentials, (c) Gibbs free energy diagram of 2e ORR and Fenton-like process on different catalyst surfaces under different applied potentials, (d) the proposed 2e ORR and Fenton-like process mechanism in the RSBC+LPBC HEF process.

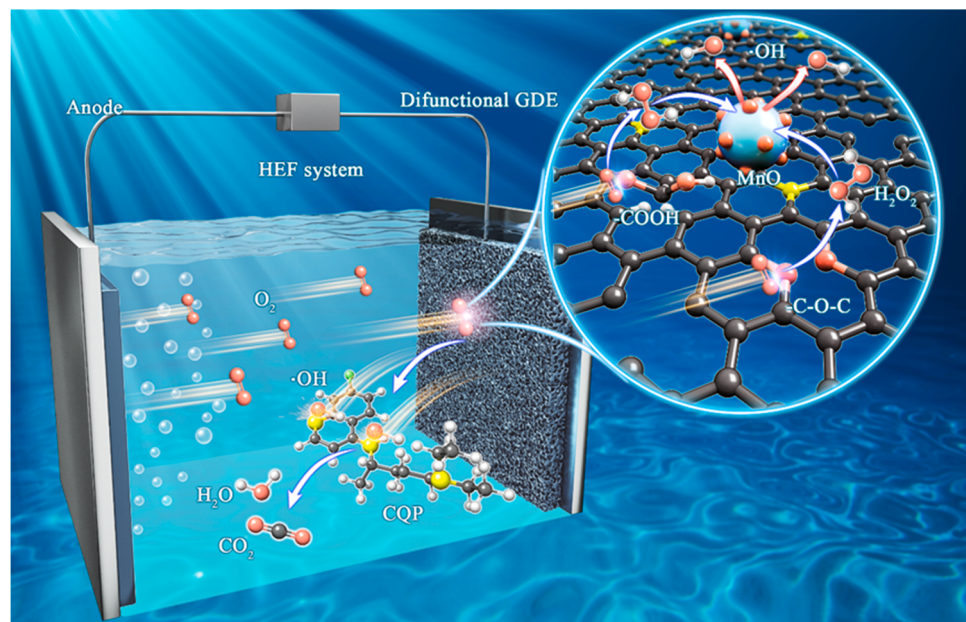


Fig. 6. Proposed mechanism for CQP degradation in RSBC+LPBC HEF system.

The *H_2O_2 would desorb and form free H_2O_2 in the absence of Mn-SAC and MnO nanoclusters near the -COOH or C-O-C sites (Fig. S32, model 1) [Eq. (4a)]. Once H_2O_2 is formed via 2e ORR, the generated H_2O_2 would be reduced to produce $\bullet OH$ via 1-electron pathway on the Mn-SAC or MnO nanocluster sites [Eq. (4b), Eq. (5)]. With the exception of the O_2 to O^* process in model 3, which was thermodynamically unfavorable (+0.18 eV), the energy changes suggested that the reduction and activation process (O_2 -to- $\bullet OH$) was more favorable on the surface of MnO nanoclusters. Thus, this process (O_2 -to- $\bullet OH$) could be represented in a schematic diagram (Fig. 5d and Fig. 6) and the following sequence:



3.5. Intermediate products and the proposed degradation pathway

The intermediate products of CQP formed during the HEF process were identified by LC-QTOF-MS/MS. It has been reported that $\bullet OH$ has a strong capacity for hydroxylating aromatic rings which leads to aldehyde groups rapidly forming carboxylic products that can attack methyl groups on aromatic rings via hydrogen abstraction for demethylation reactions [59]. The total ion current (TIC) chromatograms of the CQP oxidation in the HEF process before and after 120 min are shown in Fig. 7. The CQP has an intrinsic molecular ion peak of $m/z = 320.1884$ ($[M+H]^+$) in positive mode and 12 intermediates were detected and

summarized in Table S8. The proposed degradation pathway of CQP is shown in Fig. 7. For pathway one, P2 ($m/z = 354.1497$) and P3 ($m/z = 370.1885$) was 34 Da and 50 Da higher than CQP, which could be attributed to the addition of two or three hydroxyls (-OH) in the conjugated ring and branched chain, respectively. P2 was oxidized and released a methyl (-CH₃) and ethyl (-CH₂CH₃) at the end of the branched chain to form P4 ($m/z = 340.1781$) and P5 ($m/z = 322.1690$). The branched chain was further oxidized by breaking of the C-N bond in the amino connected with the conjugated ring to form P6 ($m/z = 223.1207$) and P7 ($m/z = 195.0898$). Additionally, a dechlorination process was also evident in degradation pathway two. P8 ($m/z = 312.1244$) and P9 ($m/z = 269.1180$) were obtained by replacing -Cl with -OH in the aromatic ring and aliphatic chain oxidation from P1. The degradation pathway of CQP also demonstrated that $\bullet OH$ was the dominant ROS in the HEF process, which was consistent with the research of Song et al. [59].

4. Conclusion

A novel one-step pyrolysis strategy has been developed to synthesize green and long-term stable dual-functional electro-catalysts from agricultural waste. The dual-functional electro-catalysts (RSBC+LPBC) exhibited superior performance for the degradation of antibiotics and dyes across a wide pH range (3–9) with outstanding stability. The synergistic effect of active sites of -COOH or C-O-C groups in the RSBC and ultra-small MnO clusters in the LPBC were the key components in converting O_2 to $\bullet OH$ via the 2e ORR and Fenton-like process, respectively, as confirmed by *operando* XAFS spectroscopy and DFT calculations. Consequently, this study reports the resource utilization of agricultural wastes to produce electro-catalysts with the potential for practical application. Moreover, the investigation of the atomic-level mechanisms suggests a new direction in the design of electro-catalysts in the HEF process.

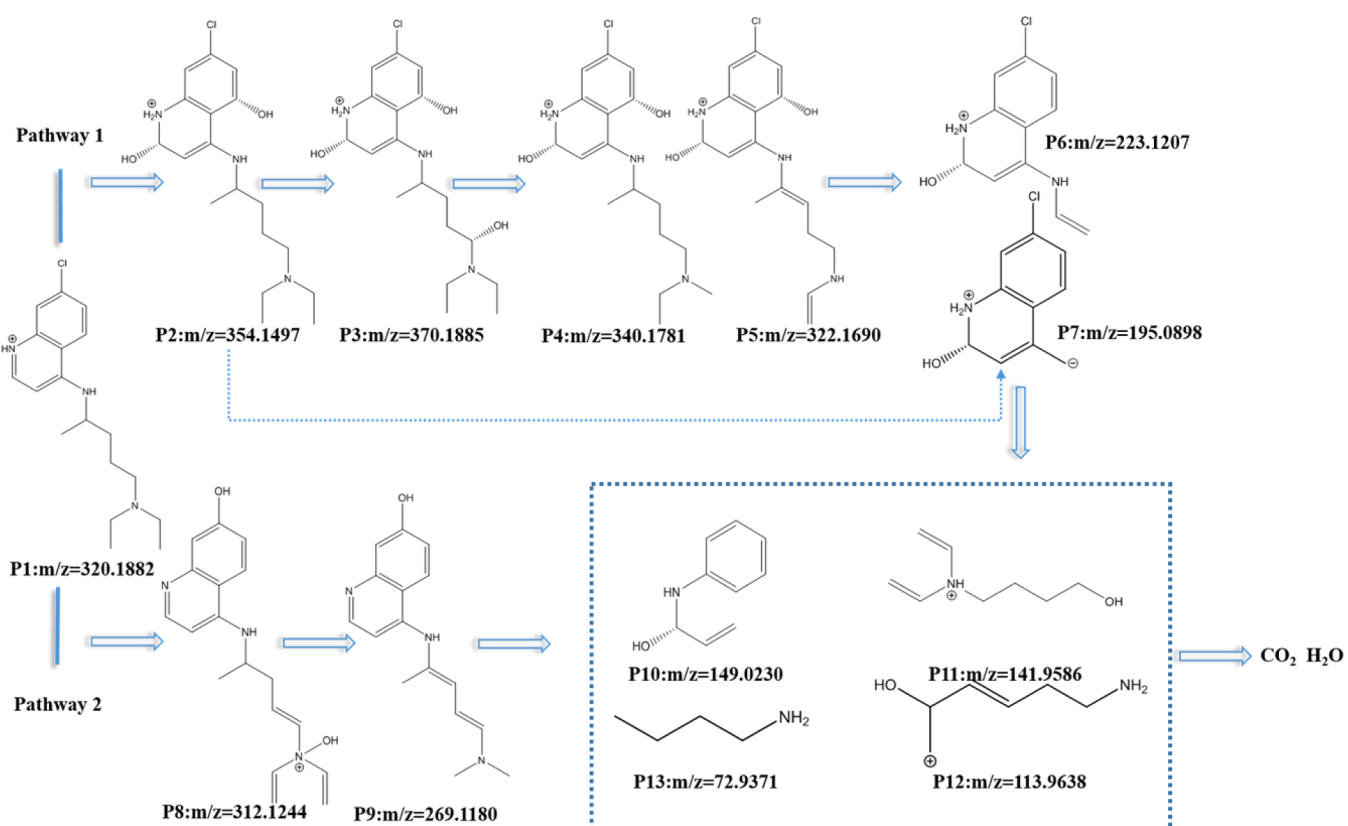


Fig. 7. Probable degradation pathway of CQP based on the analysis of the major peaks in the LC-QTOF chromatograms.

CRediT authorship contribution statement

Qiang Yang: Conceptualization, Data curation, Investigation, Writing – original draft. **Longgang Chu:** Investigation, Validation. **Tongliang Wu:** Investigation. **Yiyi Zhou:** Investigation. **Cun Liu:** Formal analysis, Validation. **Long Cang:** Project administration, Funding acquisition. **Guodong Fang:** Methodology, Supervision, Writing – review & editing. **Peixin Cui:** Project administration, Funding acquisition, Methodology, Supervision, Writing – review & editing. **Yujun Wang:** Conceptualization, Project administration, Funding acquisition, Validation.

Declaration of Competing Interest

The authors declare that they have no known competing financial interests or personal relationships that could have appeared to influence the work reported in this paper.

Data availability

Data will be made available on request.

Acknowledgements

This work was supported by the National Key Research and Development Program of China (2020YFC1806801), the National Natural Science Foundation of China (42225701, 42077145, 42107045, 41701359, 42177032), the Natural Science Foundation of Jiangsu Province (BK20211400). The authors acknowledge the staff of beamline BL14W1 and BL11B at the Shanghai Synchrotron Radiation Facility (SSRF) and engineers of DEEP-INSPECTRA X1 from Beijing SCISTAR Co. Ltd. for their support in the XAFS measurements.

Appendix A. Supporting information

Supplementary data associated with this article can be found in the online version at [doi:10.1016/j.apcatb.2023.123018](https://doi.org/10.1016/j.apcatb.2023.123018).

References

- [1] M.D.K.L. Gunathilaka, S. Bao, X. Liu, Y. Li, Y. Pan, Antibiotic pollution of planktonic ecosystems: a review focused on community analysis and the causal chain linking individual- and community-level responses, *Environ. Sci. Technol.* 57 (2023) 1199–1213, <https://doi.org/10.1021/acs.est.2c06787>.
- [2] M. Blaser, Stop the killing of beneficial bacteria, *Nature* 476 (2011) 393–394, <https://doi.org/10.1038/476393a>.
- [3] M. Huang, M. Li, F. Xiao, P. Pang, J. Liang, T. Tang, S. Liu, B. Chen, J. Shu, Y. You, Y. Li, M. Tang, J. Zhou, G. Jiang, J. Xiang, W. Hong, S. He, Z. Wang, J. Feng, C. Lin, Y. Ye, Z. Wu, Y. Li, B. Zhong, R. Sun, Z. Hong, J. Liu, H. Chen, X. Wang, Z. Li, D. Pei, L. Tian, J. Xia, S. Jiang, N. Zhong, H. Shan, Preliminary evidence from a multicenter prospective observational study of the safety and efficacy of chloroquine for the treatment of COVID-19, *Natl. Sci. Rev.* 7 (2020) 1428–1436, <https://doi.org/10.1093/nsr/nwaa113>.
- [4] X.H. Yi, H. Ji, C.C. Wang, Y. Li, Y.H. Li, C. Zhao, A. Wang, H. Fu, P. Wang, X. Zhao, W. Liu, Photocatalysis-activated SR-AOP over PDINH/MIL-88A(Fe) composites for boosted chloroquine phosphate degradation: performance, mechanism, pathway and DFT calculations, *Appl. Catal. B* 293 (2021), 120229, <https://doi.org/10.1016/j.apcatb.2021.120229>.
- [5] M. Teranishi, R. Hoshino, S.I. Naya, H. Tada, Gold-nanoparticle-loaded carbonate-modified titanium(IV) oxide surface: visible-light-driven formation of hydrogen peroxide from oxygen, *Angew. Chem. Int. Ed.* 55 (2016) 12773–12777, <https://doi.org/10.1002/ange.201606734>.
- [6] Z. Lu, G. Chen, S. Siahrostami, Z. Chen, K. Liu, J. Xie, L. Liao, T. Wu, D. Lin, Y. Liu, T.F. Jaramillo, J.K. Nørskov, Y. Cui, High-efficiency oxygen reduction to hydrogen peroxide catalysed by oxidized carbon materials, *Nat. Catal.* 1 (2018) 156–162, <https://doi.org/10.1038/s41929-017-0017-x>.
- [7] H. Sheng, R.D. Ross, J.R. Schmidt, S. Jin, Metal-compound-based electrocatalysts for hydrogen peroxide electrosynthesis and the electro-Fenton process, *ACS Energy Lett.* 8 (2023) 196–212, <https://doi.org/10.1021/acsenergylett.2c01945>.
- [8] S. Yang, A. Verdaguer-Casadevall, L. Arnarson, L. Silvoli, V. Čolić, R. Frydendal, J. Rossmeisl, I. Chorkendorff, I.E.L. Stephens, Toward the decentralized electrochemical production of H₂O₂: a focus on the catalysis, *ACS Catal.* 8 (2018) 4064–4081, <https://doi.org/10.1021/acscatal.8b00217>.
- [9] Y. Jiang, P. Ni, C. Chen, Y. Lu, P. Yang, B. Kong, A. Fisher, X. Wang, Selective electrochemical H₂O₂ production through two-electron oxygen electrochemistry, *Adv. Energy Mater.* 8 (2018), 1801909, <https://doi.org/10.1002/aenm.201801909>.
- [10] S.C. Perry, D. Pangotra, L. Vieira, L.I. Csepei, V. Sieber, L. Wang, C. Ponce de León, F.C. Walsh, Electrochemical synthesis of hydrogen peroxide from water and oxygen, *Nat. Rev. Chem.* 3 (2019) 442–458, <https://doi.org/10.1038/s41570-019-0110-6>.
- [11] Q. Zhang, M. Zhou, G. Ren, Y. Li, Y. Li, X. Du, Highly efficient electrosynthesis of hydrogen peroxide on a superhydrophobic three-phase interface by natural air diffusion, *Nat. Commun.* 11 (2020) 1731, <https://doi.org/10.1038/s41467-020-15597-y>.
- [12] K.H. Koh, A.H. Bagherzadeh Mostaghimi, Q. Chang, Y.J. Kim, S. Siahrostami, T. H. Han, Z. Chen, Elucidation and modulation of active sites in holey graphene electrocatalysts for H₂O₂ production, *EcoMat* 5 (2023), e12266, <https://doi.org/10.1002/eom2.12266>.
- [13] Y. Sun, I. Sinev, W. Ju, A. Bergmann, S. Dresp, S. Kühl, C. Spörli, H. Schmies, H. Wang, D. Bernsmeier, B. Paul, R. Schmack, R. Krahnert, B. Roldan Cuenya, P. Strasser, Efficient electrochemical hydrogen peroxide production from molecular oxygen on nitrogen-doped mesoporous carbon catalysts, *ACS Catal.* 8 (2018) 2844–2856, <https://doi.org/10.1021/acscatal.7b03464>.
- [14] J. Park, Y. Nabae, T. Hayakawa, M.A. Kakimoto, Highly selective two-electron oxygen reduction catalyzed by mesoporous nitrogen-doped carbon, *ACS Catal.* 4 (2014) 3749–3754, <https://doi.org/10.1021/cs5008206>.
- [15] V. Perazzolo, C. Durante, R. Pilot, A. Paduano, J. Zheng, G.A. Rizzi, A. Martucci, G. Granozzi, A. Gennaro, Nitrogen and sulfur doped mesoporous carbon as metal-free electrocatalysts for the in situ production of hydrogen peroxide, *Carbon* 95 (2015) 949–963, <https://doi.org/10.1016/j.carbon.2015.09.002>.
- [16] O. Scialdone, A. Galia, C. Gattuso, S. Sabatino, B. Schiavo, Effect of air pressure on the electro-generation of H₂O₂ and the abatement of organic pollutants in water by electro-Fenton process, *Electrochim. Acta* 182 (2015) 775–780, <https://doi.org/10.1016/j.electacta.2015.09.109>.
- [17] R.B. Valim, R.M. Reis, P.S. Castro, A.S. Lima, R.S. Rocha, M. Bertotti, M.R.V. Lanza, Electrogeneration of hydrogen peroxide in gas diffusion electrodes modified with tert-butyl-anthraquinone on carbon black support, *Carbon* 61 (2013) 236–244, <https://doi.org/10.1016/j.carbon.2013.04.100>.
- [18] S. Ye, J. Geng, H. Zhang, J. Hu, X. Zou, J. Li, Boosting oxygen diffusion by micro-nano bubbles for highly-efficient H₂O₂ generation on air-calcining graphite felt, *Electrochim. Acta* 439 (2023), 141708, <https://doi.org/10.1016/j.electacta.2022.141708>.
- [19] S. Guo, M. Chen, Q. Zeng, J.C.E. Yang, J. Xie, Y.X. Wang, Q. Sun, Energy-efficient H₂O₂ electro-production based on an integrated natural air-diffusion cathode and its application, *ACS EST Water* 2 (2022) 1647–1658, <https://doi.org/10.1021/acsestwater.2c00160>.
- [20] Y. Gu, S. Wu, Y. Cao, M. Liu, S. Chen, X. Quan, H. Yu, Construction of a microchannel aeration cathode for producing H₂O₂ via oxygen reduction reaction, *ACS Appl. Mater. Interfaces* 13 (2021) 56045–56053, <https://doi.org/10.1021/acsmi.1c14969>.
- [21] J. Xu, X. Zheng, Z. Feng, Z. Lu, Z. Zhang, W. Huang, Y. Li, D. Vuckovic, Y. Li, S. Dai, G. Chen, K. Wang, H. Wang, J.K. Chen, W. Mitch, Y. Cui, Organic wastewater treatment by a single-atom catalyst and electrolytically produced H₂O₂, *Nat. Sustain.* 4 (2021) 233–241, <https://doi.org/10.1038/s41893-020-00635-w>.
- [22] Q. Wang, P. Cui, Q. Yang, L. Chen, W. Wang, W. Deng, Y. Wang, Analysis of the Cd (II) adsorption performance and mechanisms by soybean root biochar: effect of pyrolysis temperatures, *Bull. Environ. Contam. Toxicol.* 107 (2021) 553–558, <https://doi.org/10.1007/s00128-021-03235-2>.
- [23] S. Tao, W. Xu, J. Zheng, F. Kong, P. Cui, D. Wu, B. Qian, S. Chen, L. Song, Soybean roots-derived N, P Co-doped mesoporous hard carbon for boosting sodium and potassium-ion batteries, *Carbon* 178 (2021) 233–242, <https://doi.org/10.1016/j.carbon.2021.03.022>.
- [24] A. Gopinath, L. Pisharody, A. Popat, P.V. Nidheesh, Supported catalysts for heterogeneous electro-Fenton processes: recent trends and future directions, *Curr. Opin. Solid State Mater. Sci.* 26 (2022), 100981, <https://doi.org/10.1016/j.cossms.2022.100981>.
- [25] S.O. Ganiyu, M. Zhou, C.A. Martinez-Huitle, Heterogeneous electro-Fenton and photoelectro-Fenton processes: a critical review of fundamental principles and application for water/wastewater treatment, *Appl. Catal. B Environ.* 235 (2018) 103–129, <https://doi.org/10.1016/j.apcatb.2018.04.044>.
- [26] L. Liu, A. Corma, Metal catalysts for heterogeneous catalysis: from single atoms to nanoclusters and nanoparticles, *Chem. Rev.* 118 (2018) 4981–5079, <https://doi.org/10.1021/cracs.7b00776>.
- [27] B. Roldan Cuenya, F. Behafarid, Nanocatalysis: size- and shape-dependent chemisorption and catalytic reactivity, *Surf. Sci. Rep.* 70 (2015) 135–187, <https://doi.org/10.1016/j.surrep.2015.01.001>.
- [28] P. Cui, C. Liu, X. Su, Q. Yang, L. Ge, M. Huang, F. Dang, T. Wu, Y. Wang, Atomically dispersed manganese on biochar derived from a hyperaccumulator for photocatalysis in organic pollution remediation, *Environ. Sci. Technol.* 56 (2022) 8034–8042, <https://doi.org/10.1021/acs.est.2c00992>.
- [29] J.T. Li, H.K. Gurajala, L.H. Wu, A. van der Ent, R.L. Qiu, A.J.M. Baker, Y.T. Tang, X. E. Yang, W.S. Shu, Hyperaccumulator plants from China: a synthesis of the current state of knowledge, *Environ. Sci. Technol.* 52 (2018) 11980–11994, <https://doi.org/10.1021/acs.est.8b01060>.
- [30] Y. Min, T. boqin, T. Meizhen, I. Aoyama, Accumulation and uptake of manganese in a hyperaccumulator *Phytolacca americana*, *Miner. Eng.* 20 (2007) 188–190, <https://doi.org/10.1016/j.mineng.2006.06.003>.

[31] X. Xu, J. Shi, X. Chen, Y. Chen, T. Hu, Chemical forms of manganese in the leaves of manganese hyperaccumulator *Phytolacca acinosa* Roxb. (Phytolaccaceae), *Plant Soil* 318 (2008) 197–204, <https://doi.org/10.1007/s11104-008-9829-4>.

[32] D.R. Fernando, T. Mizuno, I.E. Woodrow, A.J.M. Baker, R.N. Collins, Characterization of foliar manganese (Mn) in Mn (hyper) accumulators using X-ray absorption spectroscopy, *New Phytol.* 188 (2010) 1014–1027, <https://www.jstor.org/stable/40960855>.

[33] Z. Liu, K.Q. Tran, A review on disposal and utilization of phytoremediation plants containing heavy metals, *Ecotoxicol. Environ. Saf.* 226 (2021), 112821, <https://doi.org/10.1016/j.ecoenv.2021.112821>.

[34] F. Qian, X. Zhu, Y. Liu, Q. Shi, L. Wu, S. Zhang, J. Chen, Z.J. Ren, Influences of temperature and metal on subcritical hydrothermal liquefaction of hyperaccumulator: implications for the recycling of hazardous hyperaccumulators, *Environ. Sci. Technol.* 52 (2018) 2225–2234, <https://doi.org/10.1021/acs.est.7b03756>.

[35] W. Su, M. Zhao, Y. Xing, H. Ma, P. Liu, X. Li, H. Zhang, Y. Wu, C. Xia, Supercritical water gasification of hyperaccumulators for hydrogen production and heavy metal immobilization with alkali metal catalysts, *Environ. Res.* 214 (2022), 114093, <https://doi.org/10.1016/j.envres.2022.114093>.

[36] P. Wu, P. Cui, Y. Zhang, M.E. Alves, C. Liu, D. Zhou, Y. Wang, Unraveling the molecular mechanisms of Cd sorption onto MnO_x-loaded biochar produced from the Mn-hyperaccumulator *Phytolacca americana*, *J. Hazard. Mater.* 423 (2022), 127157, <https://doi.org/10.1016/j.jhazmat.2021.127157>.

[37] F. Dong, J. Li, Q. Lin, D. Wang, C. Li, Y. Shen, T. Zeng, S. Song, Oxidation of chloroquine drug by ferrate: kinetics, reaction mechanism and antibacterial activity, *Chem. Eng. J.* 428 (2022), 131408, <https://doi.org/10.1016/j.cej.2021.131408>.

[38] V. Shanmugaiah, A. Gauba, S.K. Hari, R. Prasad, V. Ramamoorthy, M.P. Sharma, Effect of silicon micronutrient on plant's cellular signaling cascades in stimulating plant growth by mitigating the environmental stressors, *Plant Growth Regul.* 100 (2023) 391–408, <https://doi.org/10.1007/s10725-023-00982-6>.

[39] B. Abebe, H.C.A. Murthy, E. Zereffa, Summary on adsorption and photocatalysis for pollutant remediation: mini review, *J. Encapsulation Adsorpt. Sci.* 08 (2018) 225–255, <https://doi.org/10.4236/jeas.2018.84012>.

[40] M. Thommes, K. Kaneko, A.V. Neimark, J.P. Olivier, F. Rodriguez-Reinoso, J. Rouquerol, K.S.W. Sing, Physisorption of gases, with special reference to the evaluation of surface area and pore size distribution (IUPAC Technical Report, *Pure Appl. Chem.* 87 (2015) 1051–1069, <https://doi.org/10.1515/pac-2014-1117>.

[41] V. Datsyuk, M. Kalyva, K. Papagelis, J. Parthenios, D. Tasis, A. Siokou, I. Kallitsis, C. Gallois, Chemical oxidation of multiwalled carbon nanotubes, *Carbon* 46 (2008) 833–840, <https://doi.org/10.1016/j.carbon.2008.02.012>.

[42] J.C. Byers, A.G. Güell, P.R. Unwin, Nanoscale electrocatalysis: visualizing oxygen reduction at pristine, kinked, and oxidized sites on individual carbon nanotubes, *J. Am. Chem. Soc.* 136 (2014) 11252–11255, <https://doi.org/10.1021/ja505708y>.

[43] Y. Liu, X. Quan, X. Fan, H. Wang, S. Chen, High-yield electrosynthesis of hydrogen peroxide from oxygen reduction by hierarchically porous carbon, *Angew. Chem. Int. Ed.* 54 (2015) 6837–6841, <https://doi.org/10.1002/ange.201502396>.

[44] S. Tan, Y. Ji, Y. Zhao, A. Zhao, B. Wang, J. Yang, J.G. Hou, Molecular oxygen adsorption behaviors on the rutile TiO₂(110)-1×1 surface: an in situ study with low-temperature scanning tunneling microscopy, *J. Am. Chem. Soc.* 133 (2011) 2002–2009, <https://doi.org/10.1021/ja110375n>.

[45] L. Guo, S. Hwang, B. Li, F. Yang, M. Wang, M. Chen, X. Yang, S.G. Karakalos, D. A. Cullen, Z. Feng, G. Wang, G. Wu, H. Xu, Promoting atomically dispersed MnN₄ sites via sulfur doping for oxygen reduction: unveiling intrinsic activity and degradation in fuel cells, *ACS Nano* 15 (2021) 6886–6899, <https://doi.org/10.1021/acsnano.0c10637>.

[46] B. Zhang, J. Zhang, J. Shi, D. Tan, L. Liu, F. Zhang, C. Lu, Z. Su, X. Tan, X. Cheng, B. Han, L. Zheng, J. Zhang, Manganese acting as a high-performance heterogeneous electrocatalyst in carbon dioxide reduction, *Nat. Commun.* 10 (2019) 2980, <https://doi.org/10.1038/s41467-019-10854-1>.

[47] A. Moraes, M.H.M.T. Assumpção, F.C. Simões, V.S. Antonin, M.R.V. Lanza, P. Hammer, M.C. Santos, Surface and catalytical effects on treated carbon materials for hydrogen peroxide electrogeneration, *Electrocatalysis* 7 (2016) 60–69, <https://doi.org/10.1007/s12678-015-0279-5>.

[48] Z. Zhou, Y. Kong, H. Tan, Q. Huang, C. Wang, Z. Pei, H. Wang, Y. Liu, Y. Wang, S. Li, X. Liao, W. Yan, S. Zhao, Cation-vacancy-enriched nickel phosphide for efficient electrosynthesis of hydrogen peroxides, *Adv. Mater.* 34 (2022), 2106541, <https://doi.org/10.1002/adma.202106541>.

[49] H. Wang, P. Li, D. Yu, Y. Zhang, Z. Wang, C. Liu, H. Qiu, Z. Liu, J. Ren, X. Qu, Unraveling the enzymatic activity of oxygenated carbon nanotubes and their application in the treatment of bacterial infections, *Nano Lett.* 18 (2018) 3344–3351, <https://doi.org/10.1021/acs.nanolett.7b05095>.

[50] A. Gopinath, L. Pisharody, A. Popat, P.V. Nidheesh, Supported catalysts for heterogeneous electro-Fenton processes: recent trends and future directions, *Curr. Opin. Solid State Mater. Sci.* 26 (2022), 100981, <https://doi.org/10.1016/j.coss.2022.100981>.

[51] Y. Gao, T. Wu, C. Yang, C. Ma, Z. Zhao, Z. Wu, S. Cao, W. Geng, Y. Wang, Y. Yao, Y. Zhang, C. Cheng, Activity trends and mechanisms in peroxyomonosulfate-assisted catalytic production of singlet oxygen over atomic metal-N-C, *Catal., Angew. Chem. Int. Ed.* 60 (2021) 22513–22521, <https://doi.org/10.1002/anie.202109530>.

[52] B. Liu, L. Guo, F. Wu, Y. Peng, J.E. Liu, T.J. Smart, N. Wang, Y.Z. Finfrock, D. Morris, P. Zhang, N. Li, P. Gao, Y. Ping, S. Chen, Ruthenium atomically dispersed in carbon outperforms platinum toward hydrogen evolution in alkaline media, *Nat. Commun.* 10 (2019) 631, <https://doi.org/10.1038/s41467-019-08419-3>.

[53] C. Chen, T. Ma, Y. Shang, B. Gao, B. Jin, H. Dan, Q. Li, Q. Yue, Y. Li, Y. Wang, X. Xu, In-situ pyrolysis of Enteromorpha as carbocatalyst for catalytic removal of organic contaminants: considering the intrinsic N/Fe in Enteromorpha and non-radical reaction, *Appl. Catal. B-Environ.* 250 (2019) 382–395, <https://doi.org/10.1016/j.apcatb.2019.03.048>.

[54] H. Song, L. Yan, J. Jiang, J. Ma, Z. Zhang, J. Zhang, P. Liu, Y. Yang, Electrochemical activation of persulfates at BDD anode: radical or nonradical oxidation? *Water Res.* 128 (2017) <https://doi.org/10.1016/j.watres.2017.10.018>.

[55] Y. Negrín-Montecelo, C. Brissaud, J.Y. Piquemal, A.O. Govorov, M.A. Correa-Duarte, L.V. Besteiro, M.J.N. Comesáñ-Hermo, Plasmonic photocatalysis in aqueous solution: assessing the contribution of thermal effects and evaluating the role of photogenerated ROS, *Nanoscale* 4 (2022) 11612–11618, <https://doi.org/10.1039/D2NR02431D>.

[56] P. Yin, X. Luo, Y. Ma, S.Q. Chu, S. Chen, X. Zheng, J. Lu, X.J. Wu, H.W. Liang, Sulfur stabilizing metal nanoclusters on carbon at high temperatures, *Nat. Commun.* 12 (2021) 3135, <https://doi.org/10.1038/s41467-021-23426-z>.

[57] P. Rao, J. Luo, D. Wu, J. Li, Q. Chen, P. Deng, Y. Shen, X. Tian, Isolated Co atoms anchored on defective nitrogen-doped carbon graphene as efficient oxygen reduction reaction electrocatalysts, *Energy Environ. Mater.* (2022), <https://doi.org/10.1002/eem2.12371>.

[58] Y. Sun, P. Cai, D. Yang, X. Yao, Single-site catalysis in heterogeneous electro-Fenton reaction for wastewater remediation, *Chem. Catal.* 2 (2022) 679–692, <https://doi.org/10.1016/j.chechat.2022.02.002>.

[59] F. Dong, J. Li, Q. Lin, D. Wang, C. Li, Y. Shen, T. Zeng, S. Song, Oxidation of chloroquine drug by ferrate: kinetics, reaction mechanism and antibacterial activity, *Chem. Eng. J.* 428 (2022), 131408, <https://doi.org/10.1016/j.cej.2021.131408>.